Electronic Supplementary Material (ESI) for Energy & Environmental Science.

Phonon-glass electron-crystal Behaviour by A site Disorder in n-Type Thermoelectric Oxides

L. M. Daniels, S. N. Savvin, M. J. Pitcher, M. S. Dyer, J. B. Claridge, S. Ling, B. Slater, F. Corà, J. Alaria* and M. J. Rosseinsky*

*Corresponding authors. Email: m.j.rosseinsky@liverpool.ac.uk, jonathan.alaria@liverpool.ac.uk

Synthesis and Processing

$La_{0.5}Na_{0.5}Ti_{1-x}Nb_xO_3$: Pre-dried reagents of La_2O_3 (Sigma Aldrich, 99.99%), Na_2CO_3 (Alfa Aesar, 99.997%), TiO_2 (Sigma Aldrich, 99.99%) and Nb_2O_5 (Alfa Aesar, 99.9985%) were weighed to give solid solutions of desired composition. All reagents were dried overnight at 473 K, except for La_2O_3, which was annealed at 1223 K. These mixtures were ground in acetone for 10 min, before being fired as a powder in an alumina crucible under air at 1273 K for 4 h using a 1 K min^{-1} heating rate and 5 K min^{-1} cooling rate. The obtained powders were ground for 10 min using a pestle and mortar, before a portion was uniaxially pressed into a 13 mm disc-shaped pellet (1 tonne, 60 s) approximately one gram in mass. The pellet was placed in an alumina boat, and buried in the remainder of the mixture which was used as sacrificial powder in order to minimise the loss of sodium during firing. This was then fired to 1573 K for 8 h under a 50 mL min^{-1} flow of H_2/N_2 (5/95%) using heating and cooling rates of 1 K min^{-1} and 5 K min^{-1}, respectively. The $p(O_2)$ was monitored during each firing under H_2/N_2 (5/95%) using a Cambridge Sensotec Rapidox 2100 Oxygen Analyser. The typical $p(O_2)$ under this atmosphere was measured to be 10^{-19} ppm (or 10^{-22} mbar). After cooling to room temperature, the pellet was separated from the sacrificial powder and then ground for characterisation.

Dense pellets were processed for property measurement by uniaxially pressing approximately one gram of the powders obtained from the first firing as described above into 13 mm disc-shaped pellets (1 tonne, 60 s) with the remaining mixture set aside to be used as sacrificial powder. The pellets were then further pressed at ambient temperature under an isostatic pressure of 200 MPa using an Autoclave Engineers Cold Isostatic Press. The pellets were placed in an alumina boat and buried in the sacrificial powder before being sintered at 1623 K for 8 h under a 50 mL min^{-1} flow of H_2/N_2 (5/95%) using heating and cooling rates of 1 K min^{-1} and 3 K min^{-1}, respectively. Pairs of pellets of each composition were processed through this method (i.e. in the same reaction); one for the measurement of electronic properties and the other for measurement of thermal conductivity. Densities of the sintered pellets were calculated using the Archimedes method.

The undoped $La_{0.5}Na_{0.5}TiO_3$ was synthesised using a procedure similar for the doped $La_{0.5}Na_{0.5}Ti_{1-x}Nb_xO_3$ series described above. The second firing, performed at 1573 K for 8 h with the pellet buried under sacrificial powder, was performed under air instead of a flow of H_2/N_2. Pairs of dense pellets for measurement were processed following the procedure described above, with the sintering step again being performed under air instead of H_2/N_2.

$Sr_{0.9}Dy_{0.1}TiO_{3-\delta}$: Pre-dried reagents of $SrCO_3$ (Alfa Aesar, 99.99%), TiO_2 (Sigma Aldrich, 99.99%) and Dy_2O_3 (Alfa Aesar, 99.99%) were weighed to give a composition of $Sr_{0.9}Dy_{0.1}TiO_3$. All reagents were dried overnight prior to weighing; $SrCO_3$ and TiO_2 at 473 K, and Dy_2O_3 at 1223 K. These mixtures were ground in acetone for 10 min, before being pressed into a 13 mm pellet (1 tonne, 60 s) and placed inside an alumina crucible before being fired at 1300 °C for 6 h in air using heating and cooling rates of 3 K min^{-1}. The pellet was then broken up and ground for 10 minutes before being uniaxially pressed into a 13 mm pellet (1 tonne, 60 s), approximately one gram in mass. The pellet was then subjected to isostatic pressing at 200 MPa using an Autoclave Engineers Cold Isostatic Press before being placed in an alumina boat on a small layer of powder of the same composition and sintered at

1773 K for 6 h under a 50 mL min^{-1} flow of H_2/N_2 (5/95%) using heating and cooling rates of 3 K min^{-1} and 3 K min^{-1}, respectively. Rietveld analysis of synchrotron X-ray diffraction (SXRD) data from $Sr_{0.9}Dy_{0.1}TiO_{3-\delta}$ showed the material to be phase pure and agree well with the structure reported previously (Fig. S13, Table S12).[1, 2]

$SrTiO_3$: Pellets of un-doped $SrTiO_3$ were prepared following a similar procedure for the doped $Sr_{0.9}Dy_{0.1}TiO_{3-\delta}$ described above. However, the isostatically pressed pellets, formed from powder following the first firing at 1573 K, were sintered under air at 1773 K instead of H_2/N_2. Rietveld analysis of SXRD data from $SrTiO_3$ showed the material to be phase pure and agree well with the structure reported previously (Fig. S13, Table S13).[3]

Characterisation

Structural analyses were performed by Rietveld refinement of synchrotron powder X-ray diffraction (SXRD), recorded at beamline I11 (λ = 0.826119 Å) at Diamond Light Source, U.K., and powder neutron diffraction (PND) data collected on HRPD at ISIS, the U.K. time-of-flight spallation neutron source. Powders were contained within borosilicate capillaries for measurement of synchrotron X-ray diffraction data. For powder neutron diffraction (PND), powders were loaded into thin-walled vanadium cylindrical cans of 8 mm diameter, and data were measured at room temperature on three detector banks (2θ = 168°, 90° and 30°). Data were corrected for absorption effects before analysis. Rietveld refinements were carried out using Topas Academic.[4] Further details of the crystal structure investigations may be obtained from the Fachinformationszentrum Karlsruhe, 76344 Eggenstein-Leopoldshafen (Germany), on quoting the depository numbers CSD-433009, CSD-433010, CSD-433011, CSD-433012. SEM images were collected using a Hitachi S-4800, cold cathode, field-emission scanning electron microscope (SEM). Samples were deposited on a carbon tape attached to an aluminium stub. Thermogravimetric analysis (TGA) was carried out using a TA Instruments Q-600. Data were measured under a 50 mL min^{-1} flow of air up to 1000 °C using a heating rate of 5 °C min^{-1} and cooling rate of 10 °C min^{-1}.

To measure the diffuse reflectance, UV-visible spectra were recorded from powders on an Agilent Cary 5000 UV-vis-NIR spectrophotometer in the wavelength range 200 -1500 nm. The Kubelka-Munk function F(R) was obtained for each sample using the reflectance R in the equation $F(R) = (1-R)^2/2R$. The Tauc method was then used to determine the direct band gaps of $SrTiO_3$, $Sr_{0.9}Dy_{0.1}TiO_3$ and $La_{0.5}Na_{0.5}Ti_{1-x}Nb_xO_3$ (where x = 0, 0.05, 0.1 and 0.2) by plotting $(h\nu F(R))^2$ against energy (Fig. S8, Table S9).

Chemical Analysis

Analysis of sample compositions was undertaken using Inductively Coupled Plasma Optical Emission Spectrometry (ICP-OES). Solutions of $La_{0.5}Na_{0.5}Ti_{1-x}Nb_xO_3$ (x = 0, 0.05, 0.1 and 0.2) were prepared by acid digestion. Approximately 10 mg of each composition were dissolved in 7 mL of concentrated HCl inside sealed Teflon-lined stainless steel autoclaves which were heated to 503 K for 3 h. These solutions were made up to 100 mL with ultra-pure water (Fisher Analytical Reagent Grade, Na < 0.05 ppm) and stored in plastic containers. Data were collected on an Agilent 5110 SVDV ICP-OES instrument.

Thermal Properties

High temperature thermal diffusivity (α) data were recorded through laser flash analysis performed on a Netzsch LFA 457. The sintered pellets (approximately 10 mm in diameter) were coated in graphitic carbon and data were collected in 50 K steps in the temperature range 295 to 943 K, with 5 min equilibration at each temperature under a 100 mL min^{-1} flow of He. The diffusivity was measured three times at each temperature and averaged; the standard deviation of these points was typically below 0.5%. Thermal expansion profiles were measured on bars approximately 4 mm in length performed on a Netzsch DIL 402C push-rod dilatometer under dynamic vacuum. Data were recorded from 298 K up to 973 K with a heating rate of 3 K min^{-1}. Heat flux profiles were measured on small pieces (30-50 mg) of sintered pellets using a Netzsch DSC 404 F1 under a 50 mL min^{-1} flow of He. Data were recorded from 323 to 973 K at a heating rate of 10 K min^{-1}. Data were measured under identical conditions from a sapphire standard of similar mass which was used to determine the heat capacities (C_p) of each sample. The thermal conductivity (κ) was calculated through combination of the diffusivity, dilatometry and heat capacity data by $\kappa(T) = \alpha(T)\cdot C_p(T)\cdot\rho(T)$, where ρ is the pellet density. The total thermal conductivity (κ_{total}) is equal to the sum of the lattice (κ_{latt}) and electronic (κ_{elec}) contributions, $\kappa_{total} = \kappa_{latt} + \kappa_{elec}$, with the electronic contribution to the thermal conductivity being estimated through the Wiedemann-Franz law,[5] $\kappa_{elec} = LT\sigma$, where L is the Sommerfield value for the Lorenz number (2.45×10^{-8} W Ω K^{-2}), T the temperature, and σ the electrical conductivity.

Low temperature thermal conductivities of $Sr_{0.9}Dy_{0.1}TiO_3$ and $SrTiO_3$ were measured on a Quantum Design Physical Property Measurement System (PPMS) on cooling and heating using the Thermal Transport Option provided by Quantum Design using bars with typical dimensions of 2 × 2 × 8 mm. Measurements from the $La_{0.5}Na_{0.5}Ti_{1-x}Nb_xO_3$ series (x = 0, 0.05, 0.1 and 0.2) with low κ were made in the 2-point geometry on dense pellets approximately 10 mm in diameter and 2 mm thick. This measurement option was chosen so as to make the thermal conductance of the sample much higher than the errors associated with the radiative heat loss.

Low temperature specific heat capacities of $Sr_{0.9}Dy_{0.1}TiO_{3-\delta}$ and $La_{0.5}Na_{0.5}Ti_{0.8}Nb_{0.2}O_3$ were measured on the PPMS using the Heat Capacity Option. Prior to taking measurements on samples, addenda tables were created. A small amount of Apiezon N Grease was placed on the sample platform and the heat capacity of the grease and the platform was measured. Afterwards, a ceramic sample was mounted on the platform by pressing it on the grease that had already been applied in order to run the addenda measurements. Typical sample mass and dimensions were 30 mg and 1.7 × 1.7 × 2.5 mm, respectively. The bars were cut on a low-speed diamond saw in a similar fashion as for the electrical property measurements outlined above and subsequently polished to improve thermal contact with the calorimeter. The sample heat capacity was obtained by subtracting the addenda table from the dataset including both the sample and the addenda.

Conductivity and thermopower measurement

High temperature electrical conductivities (σ) and Seebeck coefficients (S) were measured using rectangular bars on a ZEM-3 commercial apparatus (ULVAC-Riko). Bars with typical dimensions of 2 × 2 × 8 mm were cut using a low-speed diamond saw from sintered pellets.

The bars were mounted on a sample holder in off-axis 4-point geometry, where the inner thermocouples/voltage probes and outer current electrodes were pressed against the longer dimension or end sides of a bar respectively. The IR vacuum sample furnace was flushed with He and evacuated three times before measurement, and the residual partial pressure of He in the furnace was set to 0.01 MPa. Data were recorded both on heating and cooling using the slope method and applying temperature gradients of 10 K, 20 K and 30 K at each temperature. Consistent readings were obtained during heating and cooling cycles of the measurement, which ensured no sample degradation took place.
Low temperature electrical resistivity and Seebeck coefficients of $La_{0.5}Na_{0.5}Ti_{1-x}Nb_xO_3$ (x = 0.05, 0.1 and 0.2) and $Sr_{0.9}Dy_{0.1}TiO_3$ were measured from dense bars with typical dimensions of 2 × 2 × 8 mm cut from the same pellet as the bars for high temperature measurement described above. A silver-filled epoxy was used to affix gold-coated copper electrodes to the bars in the 4 terminal geometry. Data were recorded in continuous mode on a Quantum Design Physical Property Measurement System on cooling and heating using the Thermal Transport Option provided by Quantum Design.

Estimation of uncertainties

The standard deviations of the low temperature thermoelectric properties (κ, σ, S, C_p) were reported by the data aquisition software (DynaCool MultiVu) after estimating the goodness of of the model fits to the experimental data. The errors in the individual quantities unrelated to the transient sample response to the thermal excitation, such as heater current, sample radiation loss, thermal conductance leak, etc. were propagated using the usual quadrature formula to obtain the net standard deviation.
For the high temperature properties, the relative errors in σ, S, C_p were assumed to be about 5% as suggested by the manufacturer. This resulted in overall relative uncertainties in κ, power factors and figure of merit to be 5%, 11% and 13% respectively.

Modelling Thermal Conductivity

Modified Callaway Model for Crystalline Solids: The measured thermal conductivities of STO and SDTO were modelled using the phenomenological approach reported by Callaway.[6] Assuming the Debye approximation of constant acoustic group velocity independent of polarization is valid, the final expression for the lattice thermal conductivity is given by:

$$\kappa_{latt}(x) = \frac{k_B}{2\pi^2 v_s}\left(\frac{k_B T}{\hbar}\right)^3 \int_0^{\frac{\theta_D}{T}} \frac{x^4 e^x}{\tau_{ph}^{-1}\left(e^x - 1\right)^2} dx \qquad \text{(S1)}$$

where $x = \hbar\omega / kT$ is the variable of integration, τ_{ph}^{-1} stands for the phonon relaxation rate, ω is the phonon frequency, and v_s, $\hbar$, k_B, and θ_D are the mean velocity of sound, reduced Planck constant, Boltzmann constant, and Debye temperature, respectively. The mean sound velocities were calculated for STO and SDTO from the Debye temperatures given in Table S1 using the expression:

$$v_s = \frac{k_B \theta_D}{\hbar\sqrt[3]{6\pi^2 N}} \qquad \text{(S2)}$$

where N is the number of atom per unit volume. The total phonon scattering rate τ_{ph}^{-1} was calculated via Matthiessen's rule as a sum of inverse relaxation times each representing contribution of a particular scattering mechanism to the total thermal resistance:

$$\tau_{ph}^{-1} = \tau_B^{-1} + \tau_{pd}^{-1} + \tau_U^{-1} + \tau_{LI}^{-1} + \tau_{res}^{-1} \quad \text{(S3)}$$

where τ_B^{-1}, τ_{pd}^{-1}, τ_U^{-1}, τ_{LI}^{-1}, τ_{res}^{-1} correspond to boundary, point-defect, Umklapp, lattice imperfection, and resonance scattering, respectively. The boundary scattering relaxation rate is given by:

$$\tau_B^{-1} = \frac{v_s}{L} \quad \text{(S4)}$$

where L is the average grain size of a polycrystalline sample, is set by the microstructure of a material and contains no adjustable parameters. The average grain size of the ceramics modelled (≈10 μm) was estimated from SEM (Fig. S12) and the value of τ_B^{-1} was kept fixed during the course of the modelling.

The point-defect relaxation rate τ_{pd}^{-1} accounts for the mass contrast between foreign atoms and regular lattice sites and the strain field created by such defects. Its frequency dependence was approximated by the equation:[7]

$$\tau_{pd}^{-1} = \frac{V\omega^4}{4\pi v_s^3}\left(\sum_i f_i\left(1-\frac{m_i}{\bar{m}}\right)^2 + \sum_i f_i\left(1-\frac{r_i}{\bar{r}}\right)^2\right) = \frac{V\omega^4}{4\pi v_s^3}\cdot\Gamma = A\cdot\omega^4 \quad \text{(S5)}$$

where V is the volume per atom, ω is the phonon frequency, f_i is the fraction of atoms with mass m_i and radius r_i on a crystallographic site with average mass $\bar{m}$ and radius $\bar{r}$. Γ is the disorder scattering parameter which equates to $\Gamma = \Gamma_{MF}+\Gamma_{SF}$ where the mass fluctuation term is $\Gamma_{MF} = \sum_i f_i(1-m_i/\bar{m})^2$ and the strain field term is $\Gamma_{SF} = \sum_i f_i(1-r_i/\bar{r})^2$.

The value of the point-defect scattering pre-factor A given in Table S1 for SDTO was evaluated via Equation S5. The value of A estimated by Steigmeier was used to model the frequency dependence of τ_{pd}^{-1} for STO.[8] Just as with the boundary term, the point defect scattering pre-factors were treated as constants set by the composition of each material and were fixed to the values given in Table S1.

The contribution of the Umklapp phonon-phonon scattering to the total thermal resistance was accounted for via the empirical formula proposed by Slack:[9]

$$\tau_U^{-1} = B\omega^2 T\cdot\exp\left(-\frac{\theta_D}{3T}\right) \quad \text{(S6)}$$

where B is the constant of proportionality, which depends on θ_D and the anharmonicity of the lattice. Umklapp processes are usually dominant only at high temperatures so the value of B was adjusted to best fit κ_{latt} above 300K.

While modelling the temperature dependence of κ_{latt} for STO and SDTO it was found that the experimental data could be described more accurately if two additional terms, lattice

imperfection τ_{LI}^{-1} and resonant scattering τ_{res}^{-1} terms were included in the final expression for τ_{ph}^{-1}. The former term was shown to vary as

$$\tau_{LI}^{-1} = C \cdot \omega^2 \quad \text{(S7)}$$

and might arise either from from scattering by planar defects or defect aggregates,[10] such as stacking faults,[11] or dislocations at grain boundaries[12] or electrons-phonon scattering.[13,14] It must be noted that both electron-phonon and lattice imperfection scattering would result in identical frequency dependence of the relaxation time (Equation S7), which makes it impossible to establish the scattering mechanism underlying the ~ω^2 power law dependence unambiguously. However, given the fact that electrical conductivity of SDTO and doped LNTO was found to be strongly effected by resistive grain boundaries below 500K (Fig. S9) the above power law frequency dependence was ascribed to the lattice imperfections. It is interesting to note that the presence of terraces of growth on the surface of individual grains could be inferred from SEM images for the titanate ceramics prepared in this work (Fig. S12). Such peculiar surface structure is often due to inhomogeneous defect/impurity distribution during the sample preparation and processing.[15] It is also worth recalling that extended planar rock-salt SrO layers as in Ruddlesden-Popper phases are deemed to be a major source of phonon scattering in titanate thermoelectrics.[1] These extended defects would also result in the frequency dependence of phonon relaxation rate given by Equation S7. Inclusion of the resonant scattering term substantially improved the description of the thermal conductivity – below 70K. This was modelled by an additional relaxation time given by

$$\tau_{res}^{-1} = \frac{D \cdot \omega_0^2 \cdot \omega^2}{\left(\omega_o^2 - \omega^2\right)^2 + \gamma^2 \omega_0^2 \omega^2} \quad \text{(S8)}$$

where D is the prefactor proportional to the concentration of oscillators, which has been shown to be directly related to the amount of resonant species in a crystal, ω_o is the resonance frequency and γ is the damping factor.[16] Interestingly, the thermal conductivity of STO drops below that of SDTO on cooling, which suggests that the effective concentration of oscillators is actually higher in STO than SDTO. The same conclusion follows from the modelling as a higher value of parameter D was obtained for STO. Resonant behaviour is typically expected to scale with the amount of dopant however, Ahrens *et al*. showed that the low temperature specific heat of STO had a significant Einstein contribution on top of the Debye T^3 background, which presumably resulted from low-lying optical modes in the phonon spectrum.[17] The concentration of oscillators was estimated to be ~0.75 atoms per formula unit, which is considerably larger than in other perovkites. While modelling κ_{latt} for STO and SDTO, the resonance frequency was set to the same value as the one obtained previously.[18]

Cahill Model for Solids with Vibrational Disorder: The lower limit of thermal conductivity for STO was estimated via the model of Cahill.[18] This model describes a solid as a set of localized oscillating entities with random phases. The minimum thermal conductivity, κ_{min}, is achieved when all vibrational modes disperse at a length scale comparable to half the phonon wavelength:

$$\kappa_{\min} = \left(\frac{\pi}{6}\right)^{\frac{1}{3}} k_B N^{\frac{2}{3}} \sum_i v_i \left(\frac{T}{\theta_i}\right)^2 \int_0^{\frac{\theta_i}{T}} \frac{x^3 e^x}{\left(e^x - 1\right)^2} dx \quad \text{(S9)}$$

where N is the number density of atoms which is known from structural refinement, v_i is the sound velocity and θ_i is the cut-off frequency (in units of K) for polarization mode i. The latter have been estimated through Equation S2 using the values of longitudinal and transverse velocities of sound reported in literature.[19]

Dominant Phonon Scattering Mechanism in SDTO and LNTO

In order to estimate the effect of different scattering mechanisms in SDTO and LNTO on the lattice phonons of different frequencies the spectral lattice thermal conductivity κ_S

$$\kappa_S = \frac{k_B}{2\pi^2 v_s} \left(\frac{k_B T}{\mathrm{h}}\right)^3 \frac{x^4 e^x}{\tau_{ph}^{-1} \left(e^x - 1\right)^2} \quad \text{(S10)}$$

was calculated at 25K and 80K. The parameters given in Table S1 were used to obtain the frequency dependence of κ_S for SDTO, while in the case of undoped LNTO the low temperature part of its κ_{latt} was first fitted to Equation S1 using the modified Callaway model for crystalline solids described above. The κ_S calculated as a function of frequency for both compounds is given in Fig. S2. The mass fluctuation term results in a dramatic decrease in thermal conductivity of LNTO by disrupting phonon-mediated heat transport in a wide frequency range. In the case of SDTO the decrease in κ_S resulting from the point defects is much less pronounced and takes place in a narrower frequency range, which is in line with the retained periodicity of the force constants and phonon crystal behaviour observed therein.

Extracting Charge Carrier Concentration from Seebeck Coefficient

The temperature dependence of Seebeck coefficient of an n-type semiconductor can be obtained by solving the Boltzmann transport equation.[20] Assuming the parabolic dispersion relation for the conduction band $\epsilon = (\hbar k)^2 / 2m^*$, where k is the wave vector and m^* is the electron effective mass, and the power law energy dependence of the relaxation time $\tau = \tau_o \epsilon^{r-\frac{1}{2}}$, where r is the scattering parameter, the Seebeck coefficient due to electrons is given by

$$S = -\frac{k_B}{e}\left[\frac{(r+2)\cdot F_{r+1}(\eta^*)}{(r+1)\cdot F_r(\eta^*)} - \eta^*\right] \quad \text{(S11)}$$

where e is the elementary charge, η^* is the reduced chemical potential $\mu/k_B T$ and $F_r(\eta^*)$ is the Fermi integral

$$F_r(\eta^*) = \int_0^\infty \frac{x^r}{1 + e^{x-\eta^*}} dx \quad \text{(S12)}$$

Given that doped STO single crystals have been previously shown to have relative low Fermi temperatures (300-1300K)[21] the following formula

$$n = z\left(\frac{2\pi \cdot m^* k_B T}{h^2}\right)^{\frac{3}{2}} \frac{2}{\sqrt{\pi}} F_{\frac{1}{2}}(\eta^*) \quad \text{(S13)}$$

where $z = 6$ is the degeneracy of the conduction band, was used to estimate the electron concentration n.

Initially, the charge carrier concentration in $Sr_{0.9}Dy_{0.1}TiO_{3-\delta}$ derived from the mass gain upon reoxidation in air (Fig.S14a) was used to estimate the chemical potential via Equation S13 and to fit the temperature dependence of the Seebeck coefficient to Equation S11. This resulted in the effective mass value (Table S4) very similar to the one reported for La-doped STO.[3] In the case of $La_{0.5}Na_{0.5}Ti_{0.8}Nb_{0.2}O_3$ the same procedure gave rise to a slightly higher value of the effective mass (Table S4), which was in very good agreement with the effective masses obtained theoretically for the heavy electrons in the dispersionless bands in LNTO for the values of tilt angle ranging from 3.25° to 6.5°. Once the validity of the above approach has been tested on $Sr_{0.9}Dy_{0.1}TiO_{3-\delta}$ and $La_{0.5}Na_{0.5}Ti_{0.8}Nb_{0.2}O_3$ the concentration of charge carriers in $La_{0.5}Na_{0.5}Ti_{0.95}Nb_{0.05}O_3$ and $La_{0.5}Na_{0.5}Ti_{0.9}Nb_{0.1}O_3$ was estimated (Table S4) by fitting the temperature dependence of their respective Seebeck coefficients to Equation S11 (Fig. S9) In these fits, the charge carrier concentration was considered a free parameter, while the effective mass was set equal to that previously obtained for $La_{0.5}Na_{0.5}Ti_{0.8}Nb_{0.2}O_3$ and kept fixed during the first stages of fitting.

The mobility of the electrons at room temperature μ_{RT} (Table S4) was estimated via the expression

$$\sigma = \mu_{RT} ne \quad \text{(S14)}$$

using the values of electron concentration obtained as described above. The composition dependence of the electron concentration for Nb-doped LNTO is given in Fig. S9c.

Extracting Debye Temperatures from Heat Capacity Data

The temperature dependences of the heat capacities of $Sr_{0.9}Dy_{0.1}TiO_{3-\delta}$ and $La_{0.5}Na_{0.5}Ti_{0.8}Nb_{0.2}O_3$ were analysed in terms of Debye model, which is known to be precise at low enough temperatures where only the long wavelength acoustic phonon make a substantial contribution to the specific heat. Given the fact that both compounds were electronically conducting, the electronic contribution to their specific heat capacity was determined by fitting the isobaric heat capacity C_p below 10 K to the formula:

$$C_p = \gamma T + \beta T^3 \quad \text{(S15)}$$

where γ and β are the coefficients related to electronic and lattice specific heat, respectively. Plotting C_p/T^3 as a function of temperature revealed deviation from Debye behaviour above 10K that manifested itself as a broad peak centred at ~25 K (Fig. S3a and b). Similar low-temperature features were observed previously in $SrTiO_3$ based materials and other thermoelectrics and were believed to arise from excessive density of states due to low lying dispersionless optical modes.[17, 22-24] In such cases, the heat capacity should include an additional term to describe the contribution of independent Einstein oscillators vibrating with the same frequency:

$$C_p^E = 3R \cdot r \frac{\left(\frac{\theta_E}{T}\right)^2 \cdot \exp\left(\frac{\theta_E}{T}\right)}{\left(\exp\left(\frac{\theta_E}{T}\right) - 1\right)^2} \quad \text{(S16)}$$

where R, r and θ_E are the universal gas constant, effective number of oscillators and Einstein temperature, respectively.

The quality of fits at high temperatures were substantially improved if two Debye terms with different characteristic temperatures were used to represent the lattice part of the specific heat (Fig. S3c and d). The need to include multiple Debye terms often results from dissimilar masses and/or bonding requirements of the atoms constituting the crystal lattice. This approach was used successfully to model C_p of both oxides and molecular solids.[25, 26] The expression used to fit the temperature dependences of the heat capacities of $Sr_{0.9}Dy_{0.1}TiO_{3-\delta}$ and $La_{0.5}Na_{0.5}Ti_{0.8}Nb_{0.2}O_3$ is given by:

$$C_p = \gamma T + C_p^E + 9R\left[a \cdot \left(\frac{T}{\theta_{Da}}\right)^3 \int_0^{\frac{\theta_{Da}}{T}} \frac{x^4 e^x}{\left(e^x - 1\right)^2} dx + b \cdot \left(\frac{T}{\theta_{Db}}\right)^3 \int_0^{\frac{\theta_{Db}}{T}} \frac{x^4 e^x}{\left(e^x - 1\right)^2} dx\right] \quad \text{(S17)}$$

where γ, C_p^E, R, a, b, θ_{Da} and θ_{Db} are the Sommerfeld coefficient and Einstein contribution to specific heat defined above, universal gas constant, relative weights of each Debye term and corresponding Debye temperatures, respectively. The variable of integration is given by $x = \hbar\omega / kT$.

The extracted Debye temperatures used to model the temperature dependence of κ_{latt} were estimated by averaging:[27]

$$\theta_D = \frac{a \cdot \theta_{Da} + b \cdot \theta_{Db}}{a + b} \quad \text{(S18)}$$

The parameters used for the fitting of experimental C_p data to Equation S17 are given in Table S3.

Electronic structure calculation

All electronic band structure calculations of STO were performed using CRYSTAL14 at DFT/PBE0 level of theory.[28-29] Reciprocal space sampling has been performed for all structures using a Monkhorst- Pack grid of 8 × 8 × 8 k-points for all structures. Standard all electron basis sets from the CRYSTAL online database (www. crystal.unito.it) have been

used for O and Ti (indicated by the following labels online: O_8−411d11G_valenzano_2006, Ti_86-411(d31)G_darco_unpub). For Sr, we have used a small-core relativistic effective core potential with a double-zeta quality valence basis set (indicated by Sr_m-S-RSC_Heyd_2005_Heyd_2005 online). The initial structure of cubic STO in the rhombohedral cell (space group $R\bar{3}c$) without any octahedral tilting has been fully optimised, which was then used as the starting point to generate STO structures with octahedral tilting. The two STO structures with different amounts of octahedral tilting were manually generated, by adjusting the oxygen fractional coordinates and lattice parameters, to ensure Ti-O bond lengths remain the same. Subsequent band structure calculations were performed for the unoptimized structures (for STO with octahedral tilting). The full band structure of cubic STO (with zero tilting) is shown in Fig. S17.

Phonon calculation

The phonon calculations of STO and LNTO (with random La/Na distribution) were performed using CP2K at DFT/PBE level of theory,[30-32] using the finite-displacement method. The CP2K code employs a mixed Gaussian/plane-wave basis set, and in the current study, we employed double-ζ polarization quality Gaussian basis sets,[33] and a 400 Ry plane-wave cutoff for the auxiliary grid, in conjunction with Goedecker−Teter−Hutter pseudopotentials.[34, 35] For production quality calculations, we have used a convergence threshold of 1.0×10^{-8} Ha for the self-consistent field cycle, and structural optimizations were considered to have converged when the maximum force on all atoms falls below 1.0×10^{-4} Ha Bohr^{-1}. All calculations, including the electronic structure and phonons, were performed with the Γ-point approximation. In the finite-displacement method, the force constant, i.e the second derivatives of the total energy with respect to the atomic displacements, were computed numerically, and then the normal mode frequencies were obtained by diagonalization of the force constants matrix. In the current study, an atomic displacement of 0.01 Bohr was chosen to construct the force constants matrix. To ensure that force constants between atoms separated by large distances converge to zero, these calculations were performed in a very large rhombohedral supercell containing 640 atoms (with lattice constants ~22 Å). To characterise the difference of phonon modes in STO and LNTO, we calculated the the mean distance between those atoms that participate to the greatest extent in a given phonon mode as defined by their displacement amplitudes, denoted as d_{average}, which indicates how far the vibration propagates and is given by:

$$d_{average} = \frac{1}{n}\sum_{i,j} d_{ij} \tag{S19}$$

where i and j are atomic indices of the 10 atoms with the largest displacement amplitudes (determined from the eigenvector of a given phonon mode), d_{ij} is the distance between atoms i and j (using minimum image convention), and n is the number of pairs of atoms (from the 10 selected atoms; 45 in the current case).

Table S1. Parameters used for modelling thermal conductivity of $SrTiO_3$ (STO) and $Sr_{0.9}Dy_{0.1}TiO_{3-\delta}$ (SDTO) through the Callaway model. The Debye temperature, θ_D, and mean velocity of sound, v_s, for STO are taken from the literature.[19] These values for SDTO are extracted from fitting heat capacity data. Average grain size L, was estimated from SEM measurements. Values A, B, C, and D are all calculated constants of proportionality described in the above text. Parameter ω_o is the resonance frequency and γ is the damping factor and are obtained from modelling of the thermal conductivity data.

Material	θ_D, [K]	v_s, [m s^{-1}]	L, [μm]	A, [s^3]	B, [s K^{-1}]	C, [s]	D, [s^{-1}]	ω_o, [Hz]	γ
STO	670	5200	10	2.05×10^{-46}	2.0×10^{-18}	4.3×10^{-16}	4.6×10^{11}	3.3×10^{12}	0.9
SDTO	558	4272	10	5.00×10^{-43}	5.5×10^{-18}	4.5×10^{-16}	2.5×10^{11}	3.3×10^{12}	0.3

Table S2. Structural parameters of $La_{0.5}Na_{0.5}TiO_3$ obtained from Rietveld refinement against SXRD and high resolution NPD data (298 K). Coherent neutron scattering lengths: La = 8.24 fm, Na = 3.63 fm, Ti = -3.438 fm, and O = 5.803 fm.[33] La/Na and O sites are modelled using anisotropic displacement parameters. Space group = $R\bar{3}c$ with dimensions $a = b =$ 5.482286(6) Å, c = 13.41368(2) Å, γ = 120°, and calculated density = 5.05806(1) g cm^{-3}. Refinement statistics are R_{wp} = 2.929, R_{exp} = 1.036, χ^2 = 2.827.

Atom	Wyckoff site	x	y	z	Occupancy	100 × U_{iso} [Å^2]
La	6a	0	0	¼	0.501(3)	0.613(9)
Na	6a	0	0	¼	0.499(3)	0.613(9)
Ti	6b	0	0	0	1.00	0.517(5)
O	18e	0.54013(4)	0	¼	1.007(2)	1.115(15)
Atom	U_{11}	U_{22}	U_{33}	U_{12}	U_{13}	U_{23}
La/Na	0.00389(7)	0.00389(7)	0.01062(16)	0.00194(4)	0	0
O	0.01040(13)	0.0084(3)	0.0140(3)	0.00421(15)	-0.00247(10)	-0.0049(2)

Table S3. Parameters obtained through fitting Equation S12 to heat capacity data of $Sr_{0.9}Dy_{0.1}TiO_{3-\delta}$ and $La_{0.5}Na_{0.5}Ti_{0.8}Nb_{0.2}O_3$.

Material	γ [J mol^{-1} K^{-2}]	θ_E [K]	r	A	θ_{Da} [K]	b	θ_{Db} [K]	θ_D [K]
$Sr_{0.9}Dy_{0.1}TiO_{3-\delta}$	1.34×10^{-2}	144	0.1	1	232	3.533	650	558
$La_{0.5}Na_{0.5}Ti_{0.8}Nb_{0.2}O_3$	4.5×10^{-3}	137	0.45	1	280	3.433	700	605

Table S4. Electron concentration n, effective mass m^* and room temperature mobility μ_{RT} for $Sr_{0.9}Dy_{0.1}TiO_{3-\delta}$ and $La_{0.5}Na_{0.5}Ti_{1-x}Nb_xO_3$. The values of n and m^* were extracted by fitting the temperature dependence of the Seebeck coefficient to Equation S11 , while μ_{RT} was calculated using Equation S14.

Material	n, [cm^{-3}]	m^*/m_o	μ_{RT}, [$cm^2\ V^{-1}\ s^{-1}$]
$Sr_{0.9}Dy_{0.1}TiO_{3-\delta}$	14×10^{20}	1.60	0.5
$La_{0.5}Na_{0.5}Ti_{0.95}Nb_{0.05}O_3$	7×10^{20}	2.15	1.0
$La_{0.5}Na_{0.5}Ti_{0.9}Nb_{0.1}O_3$	16×10^{20}	2.25	0.6
$La_{0.5}Na_{0.5}Ti_{0.8}Nb_{0.2}O_3$	32×10^{20}	2.23	0.8

Table S5. Bond distances and angles as a function of Nb^{5+} substitution in the $La_{0.5}Na_{0.5}Ti_{1-x}Nb_xO_3$ series obtained from Rietveld refinement against room temperature SXRD and high resolution NPD data.

x	A–O [Å]	Average A–O [Å]	B–O [Å]	A–O/B–O	B–O–B [°]	ϕ [°]
0.0	3 × 2.5213(3), 6 × 2.74784(3), 3 × 2.9613(3)	2.7446(2)	1.95003(4)	1.4075	167.044(14)	7.914(10)
0.05	3 × 2.5311(7), 6 × 2.75380(7), 3 × 2.9629(7)	2.7504(4)	1.95378(10)	1.4077	167.31(4)	7.75(3)
0.10	3 × 2.54114(7), 6 × 2.75752(7), 3 × 2.95726(7)	2.7534(4)	1.95524(10)	1.4082	167.78(4)	7.45(3)
0.20	3 × 2.5525(10), 6 × 2.76119(9), 3 × 2.9555(10)	2.7576(5)	1.95771(13)	1.4086	168.19(4)	7.22(2)

Table S6. Structural parameters of $La_{0.5}Na_{0.5}Ti_{0.8}Nb_{0.2}O_3$ obtained from Rietveld refinement against SXRD and high resolution NPD data (298 K). Coherent neutron scattering lengths: La = 8.24 fm, Na = 3.63 fm, Ti = -3.438 fm, Nb = 7.054 fm, and O = 5.803 fm.[37] La/Na and O sites are modelled using anisotropic displacement parameters. Space group = $R\bar{3}c$ with dimensions $a = b = 5.508739(13)$ Å, $c = 13.49234(8)$ Å, $\gamma = 120°$, and calculated density = 5.22116(4) g cm^{-3}. Refinement statistics are $R_{wp} = 3.863$, $R_{exp} = 1.089$, $\chi^2 = 3.546$.

Atom	Wyckoff site	X	y	z	Occupancy	$100 \times U_{iso}$ [Å^2]
La	6a	0	0	¼	0.4992(16)	0.91(3)
Na	6a	0	0	¼	0.5008(16)	0.91(3)
Ti	6b	0	0	0	0.8	0.27(5)
Nb	6b	0	0	0	0.2	0.27(5)
O	18e	0.53658(10)	0	¼	0.998(4)	1.67(5)
Atom	U_{11}	U_{22}	U_{33}	U_{12}	U_{13}	U_{23}
La/Na	0.0059(3)	0.0059(3)	0.01533(5)	0.0029(3)	0	0
O	0.0114(4)	0.0196(16)	0.0219(13)	0.0098(8)	-0.0067(3)	-0.0134(7)

Table S7. Structural parameters of $La_{0.5}Na_{0.5}Ti_{0.95}Nb_{0.05}O_3$ from Rietveld refinement against SXRD data only (298 K). Space group = $R\bar{3}c$ with dimensions $a = b = 5.493959(7)$ Å, $c = 13.44522(4)$ Å, $\gamma = 120°$, and calculated density = 5.07375(2) g cm^{-3}. Refinement statistics are $R_{wp} = 2.247$, $R_{exp} = 0.854$, $\chi^2 = 2.631$.

Atom	Wyckoff site	X	y	z	Occupancy	$100 \times U_{iso}$ [Å^2]
La	6a	0	0	¼	0.4996(5)	0.325(4)
Na	6a	0	0	¼	0.5004(5)	0.325(4)
Ti	6b	0	0	0	0.95	0.307(5)
Nb	6b	0	0	0	0.05	0.307(5)
O	18e	0.53929(13)	0	¼	1.0	0.954(17)

Table S8. Structural parameters of $La_{0.5}Na_{0.5}Ti_{0.9}Nb_{0.1}O_3$ from Rietveld refinement against SXRD data only (298 K). Space group = $R\bar{3}c$ with dimensions $a = b = 5.49881(6)$ Å, $c = 13.46880(16)$ Å, $\gamma = 120°$, and calculated density = 5.10018(15) g cm^{-3}. Refinement statistics are $R_{wp} = 2.451$, $R_{exp} = 0.889$, $\chi^2 = 2.757$.

Atom	Wyckoff site	X	y	z	Occupancy	100 × U_{iso} [Å^2]
La	6a	0	0	¼	0.4933(5)	0.397(3)
Na	6a	0	0	¼	0.5067(5)	0.397(3)
Ti	6b	0	0	0	0.9	0.363(4)
Nb	6b	0	0	0	0.1	0.363(4)
O	18e	0.53784(13)	0	¼	1.0	1.123(15)

Table S9. Band gap energies obtained from direct Tauc plots of diffuse reflectance data for each material measured in this study.

Material	Direct Tauc Band Gap [eV]
$SrTiO_3$	3.27(5)
$Sr_{0.9}Dy_{0.1}TiO_{3-\delta}$	3.29(4)
$La_{0.5}Na_{0.5}TiO_3$	3.32(4)
$La_{0.5}Na_{0.5}Ti_{0.95}Nb_{0.05}O_3$	3.24(3)
$La_{0.5}Na_{0.5}Ti_{0.9}Nb_{0.1}O_3$	3.24(5)
$La_{0.5}Na_{0.5}Ti_{0.8}Nb_{0.2}O_3$	3.12(5)

Table S10. Results of ICP-OES measurements on $La_{0.5}Na_{0.5}Ti_{1-x}Nb_xO_3$ materials. Concentrations have been normalized to titanium for comparison with the nominal stoichiometric compositions. Absolute errors are shown.

Composition	La	Na	Ti	Nb
$La_{0.5}Na_{0.5}TiO_3$	0.492(2)	0.495(7)	1.000(3)	–
$La_{0.5}Na_{0.5}Ti_{0.95}Nb_{0.05}O_3$	0.490(2)	0.472(8)	0.950(4)	0.048(1)
$La_{0.5}Na_{0.5}Ti_{0.9}Nb_{0.1}O_3$	0.488(7)	0.459(8)	0.900(3)	0.096(2)
$La_{0.5}Na_{0.5}Ti_{0.8}Nb_{0.2}O_3$	0.538(8)	0.471(7)	0.800(4)	0.206(1)

Table S11. Theoretical (obtained from Rietveld refinement) and experimental densities of sintered pellets for each material measured in this study.

Material	Theoretical density [g cm^{-3}]	Experimental density [%]
$SrTiO_3$	5.13350(1)	98.8
$Sr_{0.9}Dy_{0.1}TiO_{3-\delta}$	5.3112(12)	94.9
$La_{0.5}Na_{0.5}TiO_3$	5.05147(1)	98.0
$La_{0.5}Na_{0.5}Ti_{0.95}Nb_{0.05}O_3$	5.07375(2)	98.0
$La_{0.5}Na_{0.5}Ti_{0.9}Nb_{0.1}O_3$	5.10018(15)	97.0
$La_{0.5}Na_{0.5}Ti_{0.8}Nb_{0.2}O_3$	5.22116(4)	98.0

Table S12. Structural parameters of $Sr_{0.1}Dy_{0.1}TiO_3$ from Rietveld refinement against SXRD data (298 K). Space group = *I*4/*mcm* with dimensions $a = b = 5.511809(5)$ Å, $c = 7.809766(11)$ Å, and calculated density = 5.3112(12) g cm^{-3}. Refinement statistics are $R_{wp} = 3.026$, $R_{exp} = 1.098$, $\chi^2 = 2.756$.

Atom	Wyckoff site	X	y	z	Occupancy	100 × U_{iso} [Å^2]
Sr	4b	0	½	¼	0.9110(6)	0.668(3)
Dy	4b	0	½	¼	0.0889(6)	0.668(3)
Ti	4c	0	0	0	1.0	0.122(4)
O	4a	0	0	¼	0.984(3)	0.64(4)
O	8h	0.26960(13)	0.76960(13)	0	0.9944(17)	1.17(3)

Table S13. Structural parameters of $SrTiO_3$ from Rietveld refinement against SXRD data (298 K). Space group = $Pm\bar{3}m$ with dimensions a = 3.909149(3) Å and calculated density = 5.13350(1) g cm^{-3}. Refinement statistics are R_{wp} = 2.924, R_{exp} = 1.420, χ^2 = 2.059.

Atom	Wyckoff site	X	y	z	Occupancy	100 × U_{iso} [Å^2]
Sr	1a	0	0	0	0.994(8)	0.449(2)
Ti	1b	½	½	½	1.0351(8)	0.303(3)
O	3c	0	½	½	1.0	0.639(6)

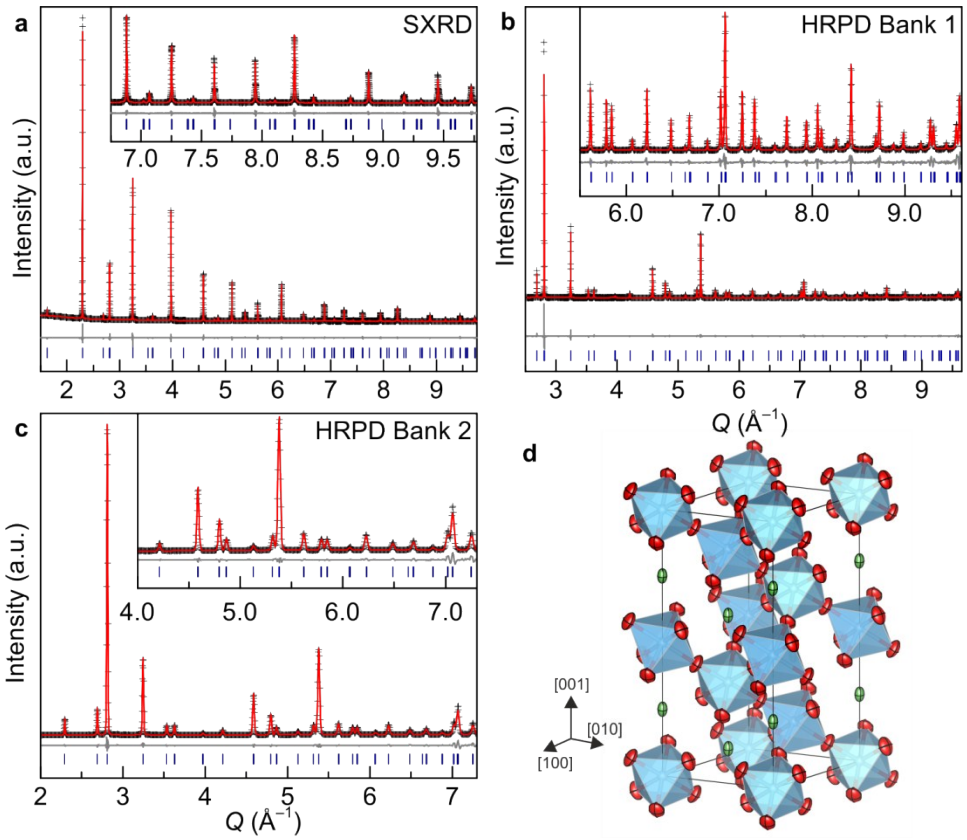

Fig. S1. Rietveld refinements against a) SXRD (λ = 0.826119 Å) and high resolution NPD data measured on b) Bank 1 (backscattering 2θ = 168°) and c) Bank 2 (2θ = 90° bank) of HRPD at room temperature for $La_{0.5}Na_{0.5}TiO_3$.

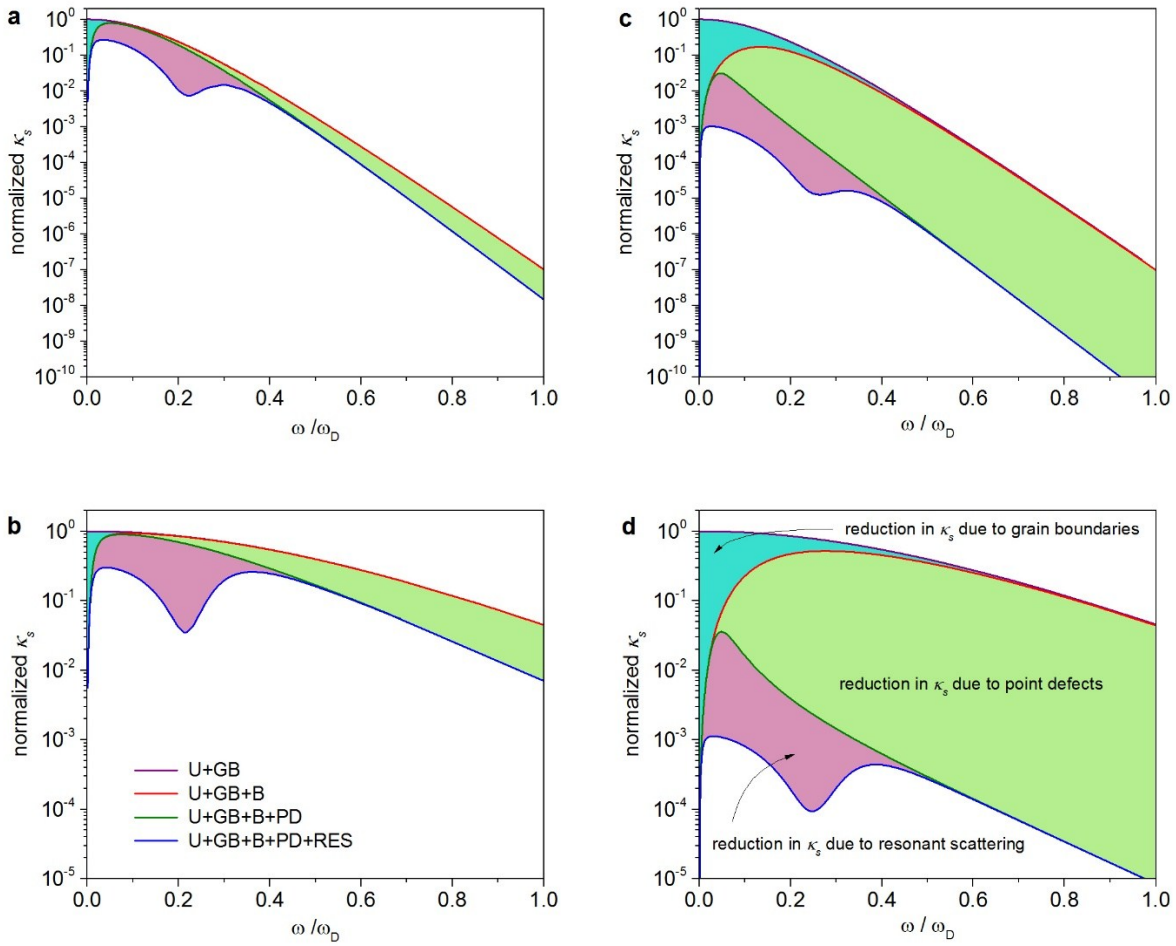

Fig. S2. Calculated spectral thermal conductivity κ_S for $Sr_{0.9}Dy_{0.1}TiO_{3-\delta}$ at a) 25 K and b) 80 K and $La_{0.5}Na_{0.5}TiO_3$ at c) 25 K and d) 80 K, illustrating the contribution of different scattering mechanisms in decreasing κ_S (cyan: grain boundaries, green: point defects and purple: resonant scattering).

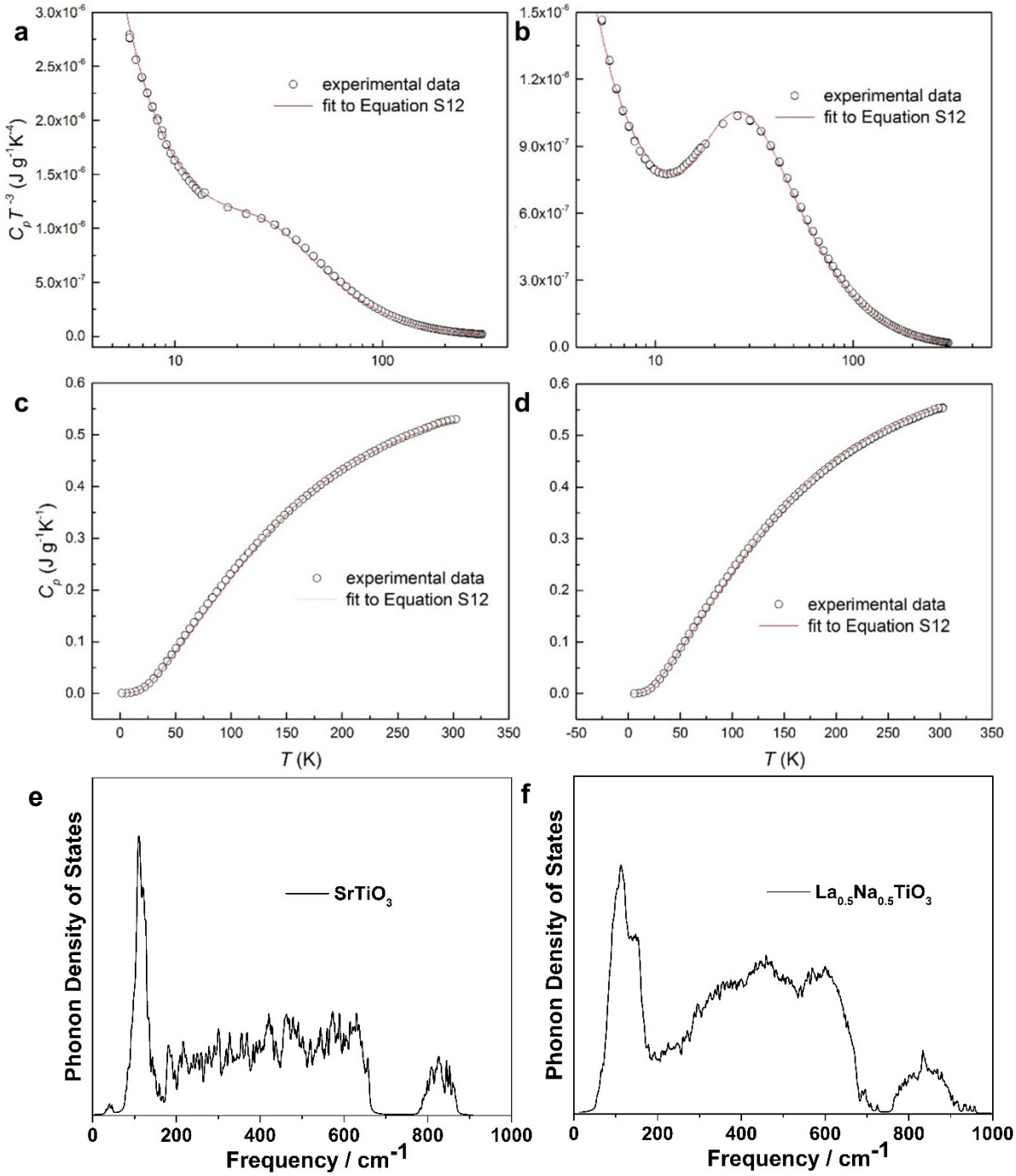

Fig. S3. Plots of C_p/T^3 against T for a) $Sr_{0.9}Dy_{0.1}TiO_{3-\delta}$ and b) $La_{0.5}Na_{0.5}Ti_{0.8}Nb_{0.2}O_3$ illustrating the non-Debye behaviour around ~25 K. Specific heat capacity data of c) $Sr_{0.9}Dy_{0.1}TiO_{3-\delta}$ and d) $La_{0.5}Na_{0.5}Ti_{0.8}Nb_{0.2}O_3$ as a function of temperature. Red lines represent fits to the data using Equation S12. Density of states derived from the phonon calculations for $SrTiO_3$ and $La_{0.5}Na_{0.5}TiO_3$ highlighting the low-frequency excess density of states. The phonon density of states have been broadened using a Lorentzian line shape function, with a half width of 2 cm^{-1}.

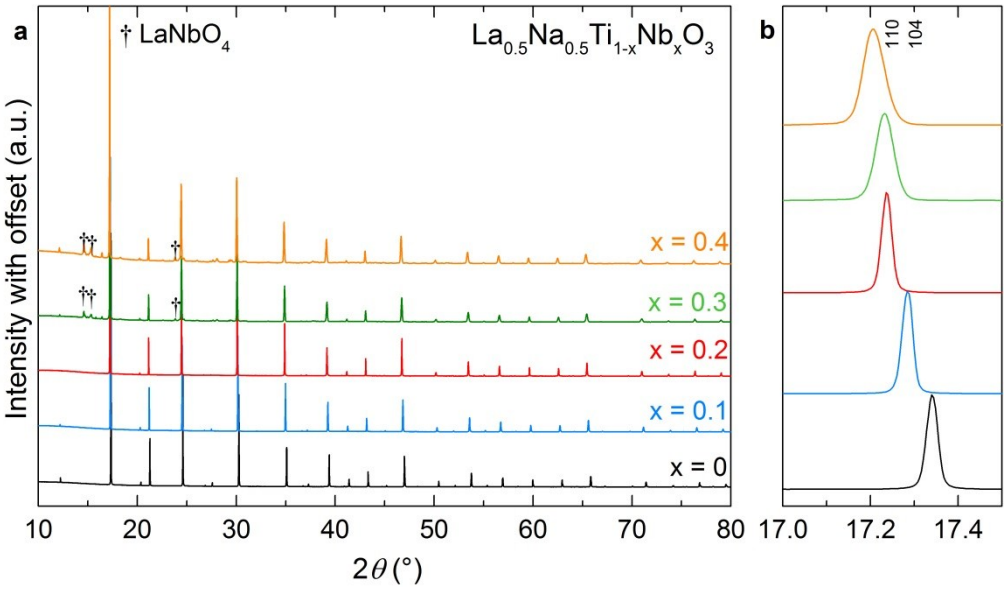

Fig. S4. SXRD (λ = 0.826119 Å) data measured on samples in the composition range $La_{0.5}Na_{0.5}Ti_{1-x}Nb_xO_3$. Pure samples were obtained up to x = 0.2, above which small amounts of $LaNbO_4$ were observed. Composition dependence of the position of the 110 and 104 reflections is highlighted in b).

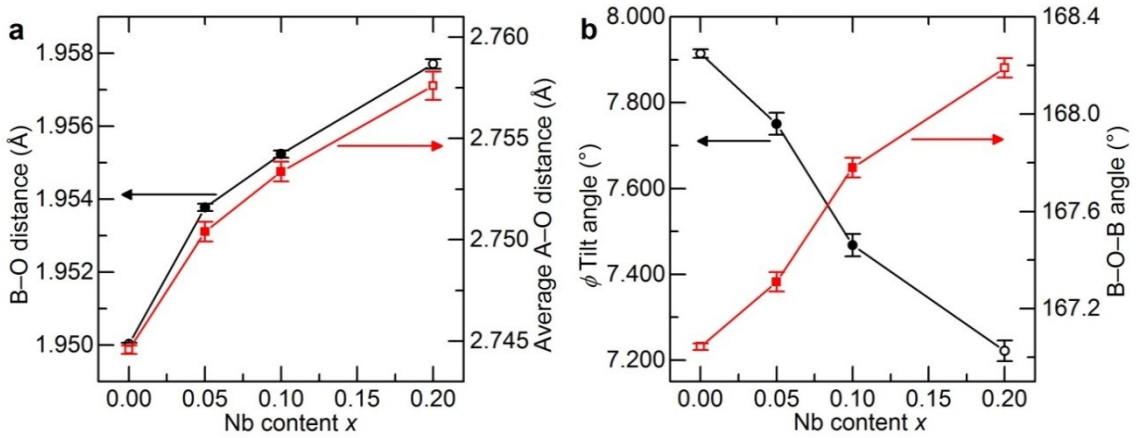

Fig. S5. Variation of a) octahedral tilt angle, ϕ, and B–O–B angle and b) B–O and average A–O distances as a function of x in $La_{0.5}Na_{0.5}Ti_{1-x}Nb_xO_3$. Octahedral tilt angles were determined through $\phi = \arctan[2\sqrt{3}(x–0.5)]$, where x is the x-coordinate of the 18*e* oxide ion.[38] Hollow points show materials studied through Rietveld refinement of both SXRD and high resolution NPD data, whilst filled points involved analysis of SXRD data only.

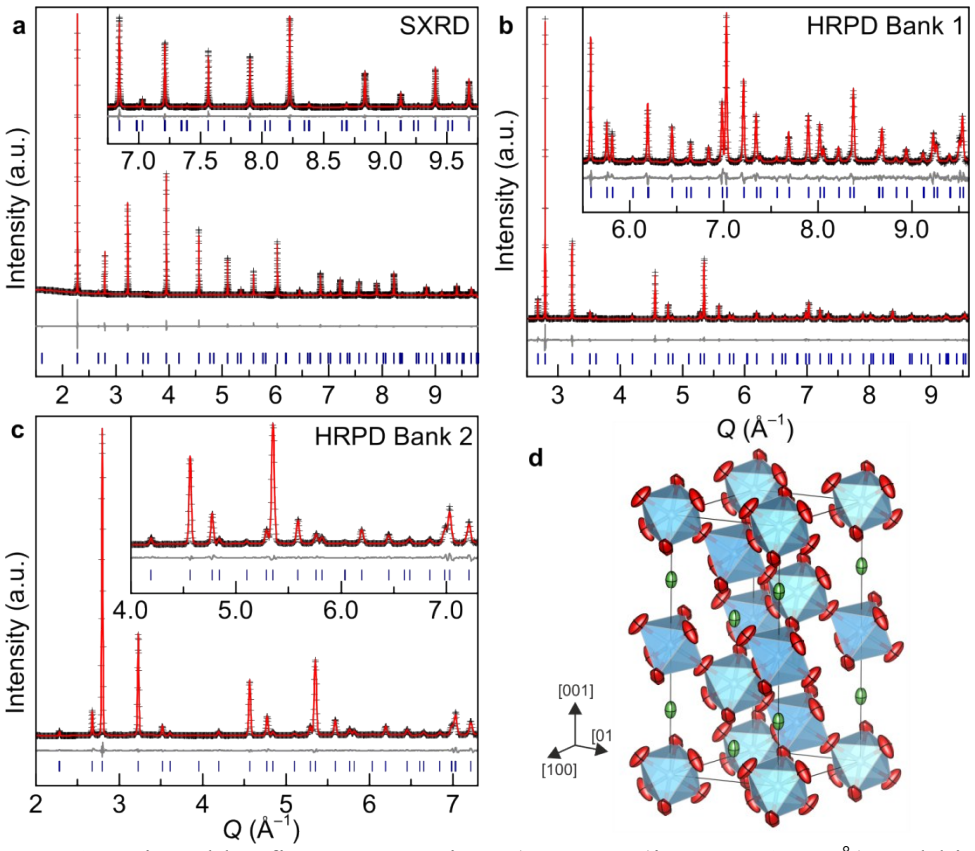

Fig. S6. Rietveld refinements against a) SXRD (λ = 0.826119 Å) and high resolution NPD data measured on b) Bank 1 (backscattering 2θ = 168°) and c) Bank 2 (2θ = 90° bank) of HRPD at room temperature for $La_{0.5}Na_{0.5}Ti_{0.8}Nb_{0.2}O_3$.

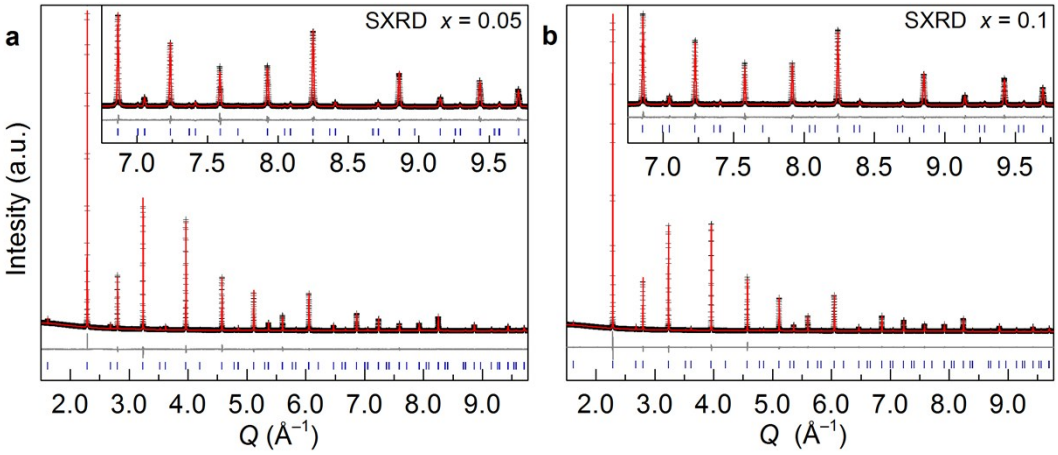

Fig. S7. Rietveld refinements made against SXRD (λ = 0.826119 Å) data for the a) x = 0.05 and b) x = 0.1 doped materials in the $La_{0.5}Na_{0.5}Ti_{1-x}Nb_xO_3$ solid solution.

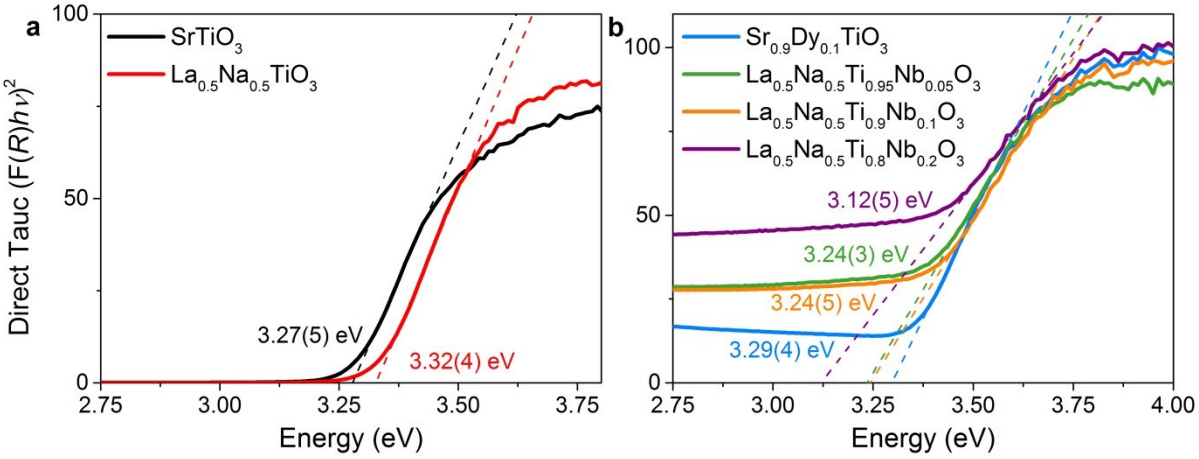

Figure S8. Tauc plots of direct band gaps calculated using the Kubelka-Munk function F(*R*) obtained from diffuse reflectance measurements for a) $SrTiO_3$ and $La_{0.5}Na_{0.5}TiO_3$, and b) $Sr_{0.9}Dy_{0.1}TiO_3$, and $La_{0.5}Na_{0.5}Ti_{1-x}Nb_xO_3$ (where x = 0.05, 0.1 and 0.2).

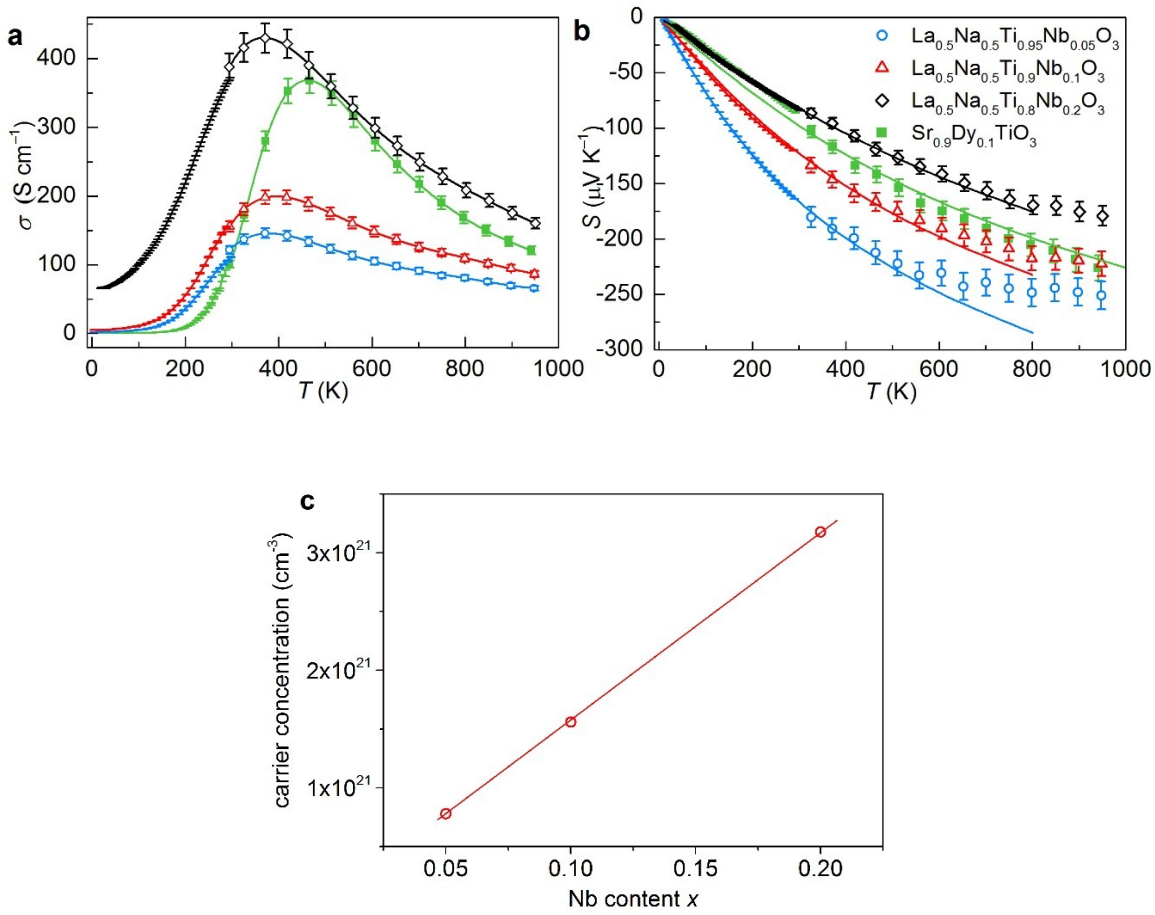

Fig. S9. Temperature dependence of a) electrical conductivity, σ, and b) Seebeck coefficient, S, for $La_{0.5}Na_{0.5}Ti_{1-x}Nb_xO_3$, where x = 0.05 (blue circles), 0.1 (red triangles) and 0.2 (black diamonds). Solid lines in b) show the results calculated using Equation S11. Data measured from $Sr_{0.9}Dy_{0.1}TiO_{3-\delta}$ (green squares) are included for comparison purposes. c) Composition dependence of charge carrier concentration in $La_{0.5}Na_{0.5}Ti_{1-x}Nb_xO_3$.

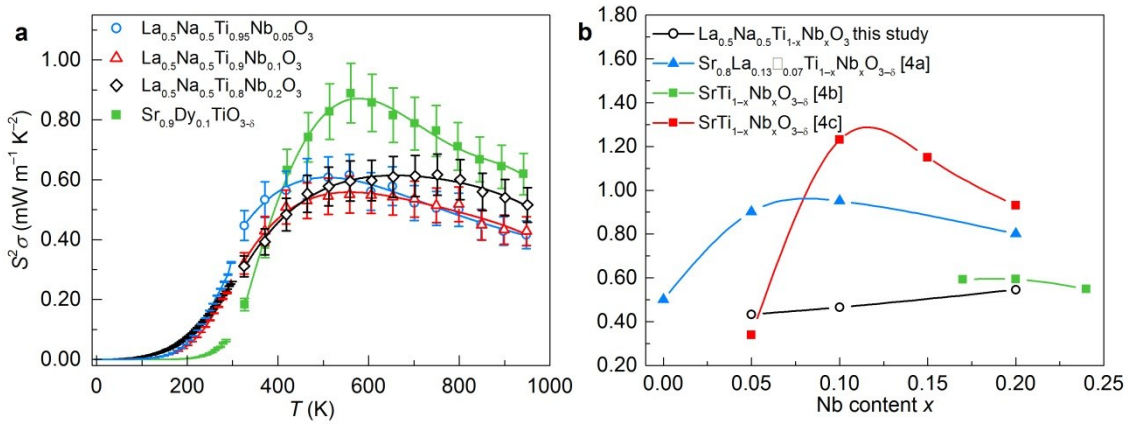

Fig. S10. Temperature dependence of power factors ($S^2\sigma$) for $La_{0.5}Na_{0.5}Ti_{1-x}Nb_xO_3$ a), where x = 0.05 (blue circles), 0.1 (red triangles) and 0.2 (black diamonds). Data measured from $Sr_{0.9}Dy_{0.1}TiO_{3-\delta}$ (green squares) are included for comparison purposes. Comparison of power factor as a function of x b) for $La_{0.5}Na_{0.5}Ti_{1-x}Nb_xO_3$ against data reported previously for $SrTi_{1-x}Nb_xO_3$ bulk materials at 900 K. Data are taken from the references shown in the key.[39-41]

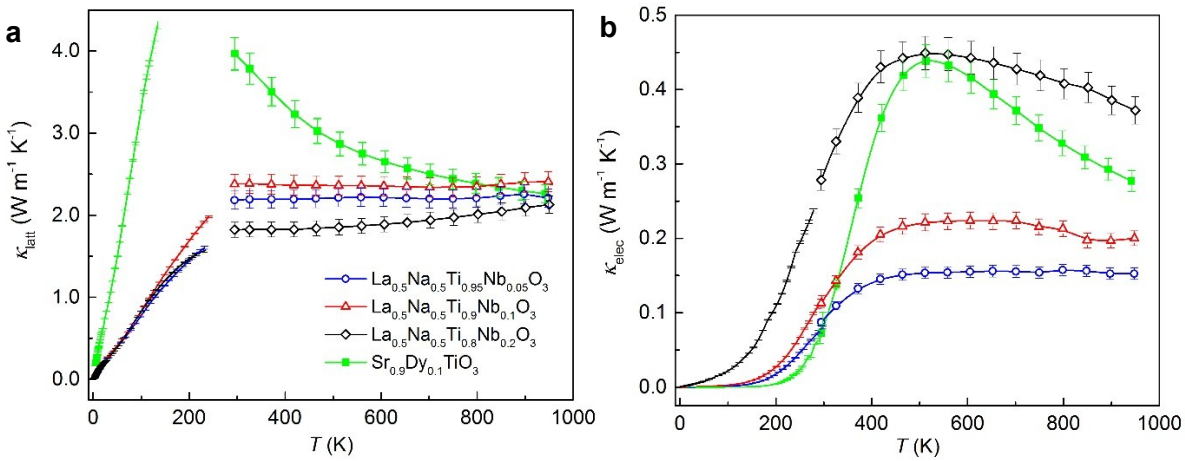

Fig. S11. Temperature dependence of a) κ_{latt} and b) κ_{elec} contributions to the thermal conductivity for $La_{0.5}Na_{0.5}Ti_{1-x}Nb_xO_3$, where x = 0.05 (blue circles), 0.1 (red triangles) and 0.2 (black diamonds). Data measured from $Sr_{0.9}Dy_{0.1}TiO_{3-\delta}$ (green squares) are included for comparison purposes. The electronic contribution to κ was estimated using the Wiedemann-Franz law.[5]

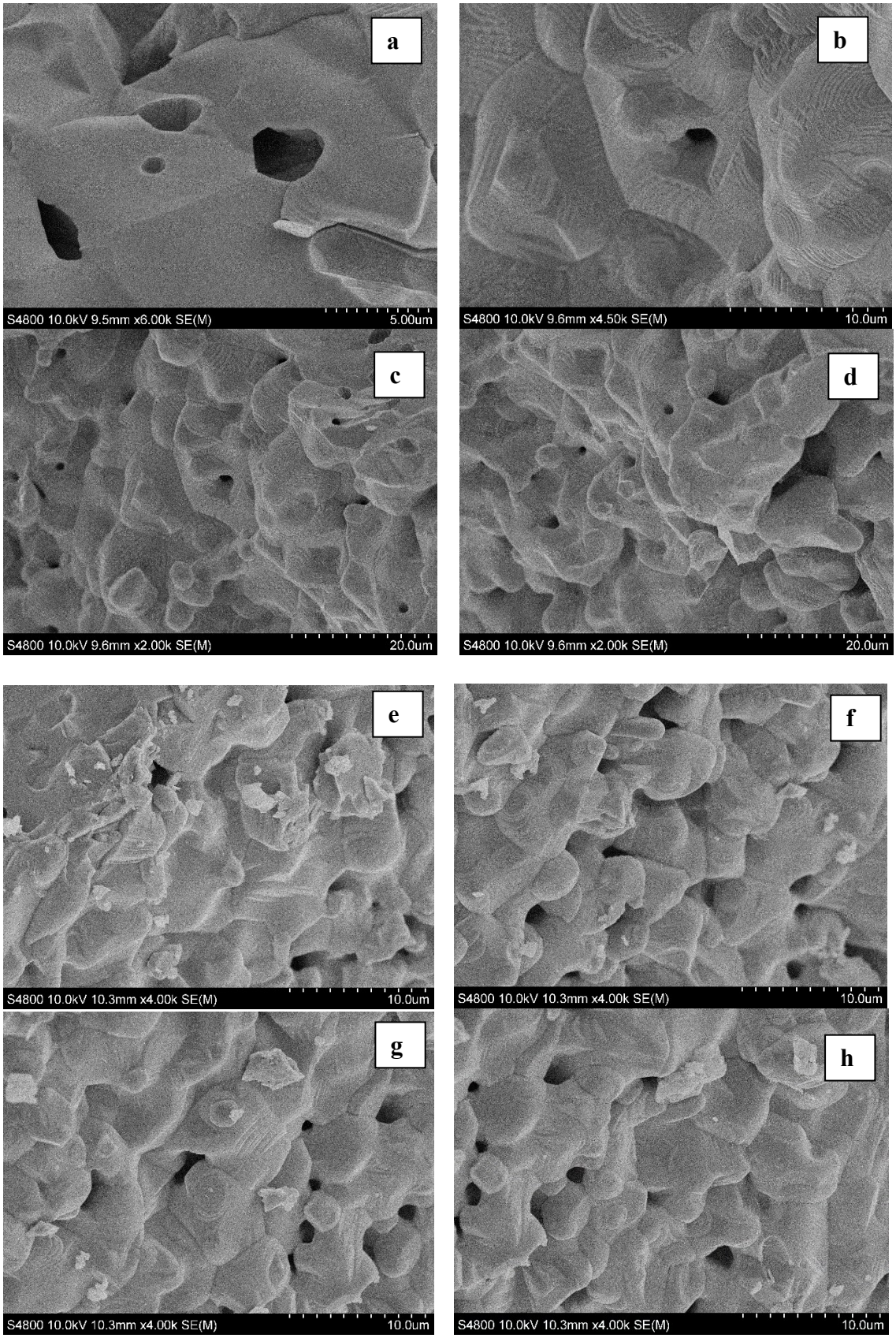

Fig. S12. Scanning electron micrograph images for $Sr_{0.9}Dy_{0.1}TiO_{3-\delta}$ (a-d) and $La_{0.5}Na_{0.5}Ti_{0.8}Nb_{0.2}O_3$ (e-h).

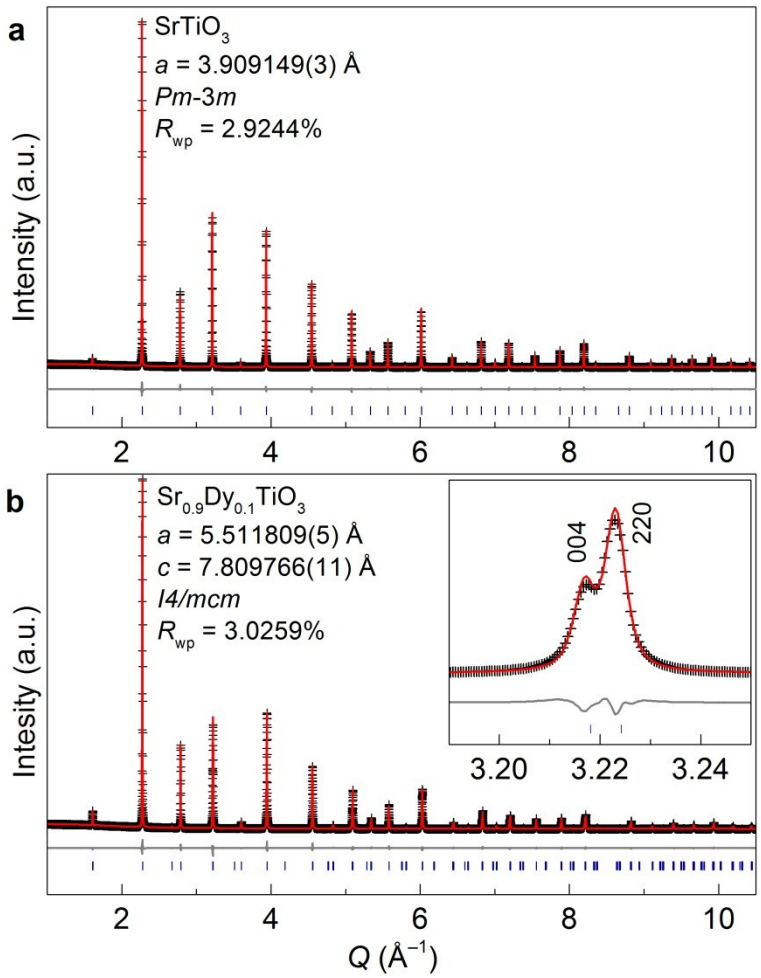

Fig. S13. Rietveld refinements against SXRD (λ = 0.826119 Å) data measured from a) $SrTiO_3$ and b) $Sr_{0.9}Dy_{0.1}TiO_3$. The inset in b) shows the splitting of the 004 and 220 reflections in tetragonal $Sr_{0.9}Dy_{0.1}TiO_3$.

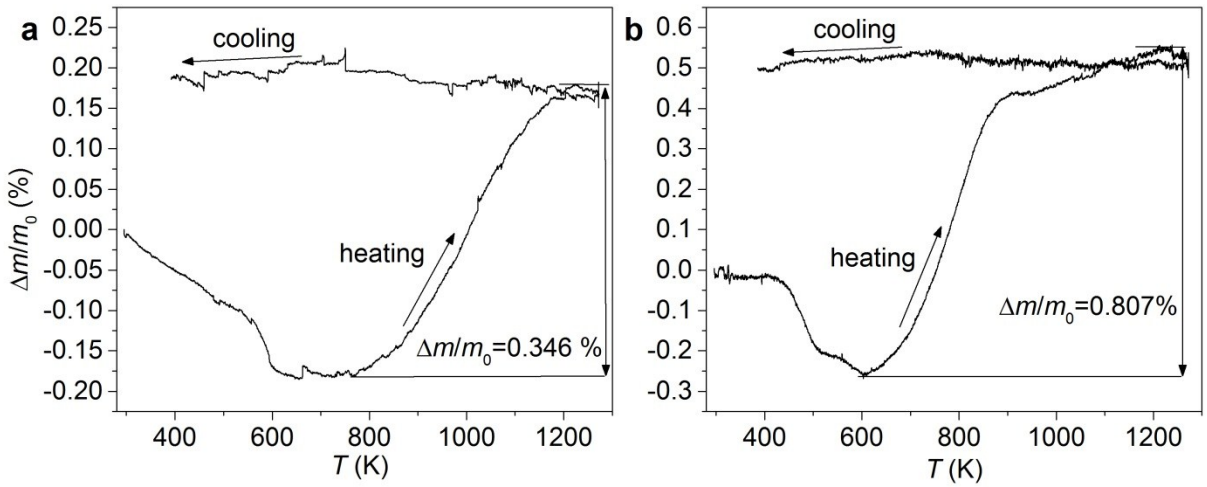

Fig. S14. Relative weight change for a) $Sr_{0.9}Dy_{0.1}TiO_3$ and b) $La_{0.5}Na_{0.5}Ti_{0.8}Nb_{0.2}O_3$ as a result of oxidation from heating up to 1273 K under air. The data show oxidation to take place at approximately 750 K and 600 K for $Sr_{0.9}Dy_{0.1}TiO_3$ and $La_{0.5}Na_{0.5}Ti_{0.8}Nb_{0.2}O_3$, respectively. The materials were white in colour after cooling to room temperature.

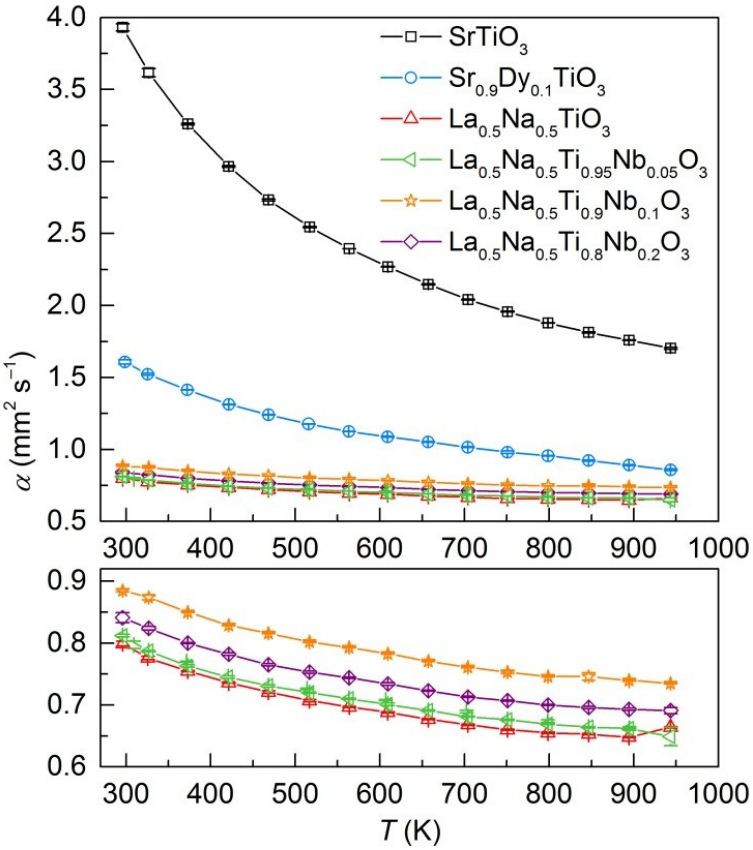

Fig. S15. Temperature dependence of the thermal diffusivity (α) for all materials in this study.

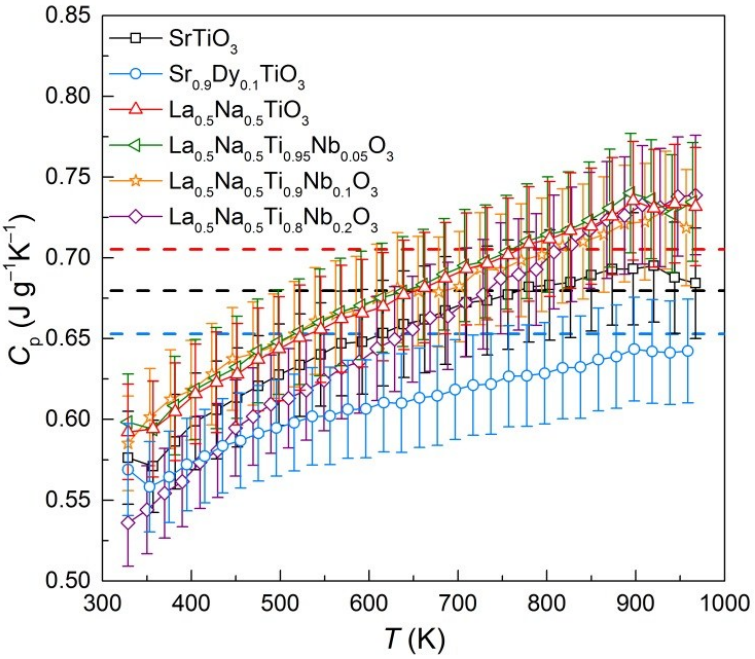

Fig. S16. Temperature dependence of the specific heat capacity (C_p) for all materials in this study. Error bars show 5% uncertainty. Dashed lines represent C_p values for STO (black), SDTO (blue), and LNTO (red) estimated from the Dulong-Petit law, $C_p = 3nR$, where R is the molar gas constant, 8.314 J K^{-1} mol^{-1} and n is the number of atoms per unit volume.

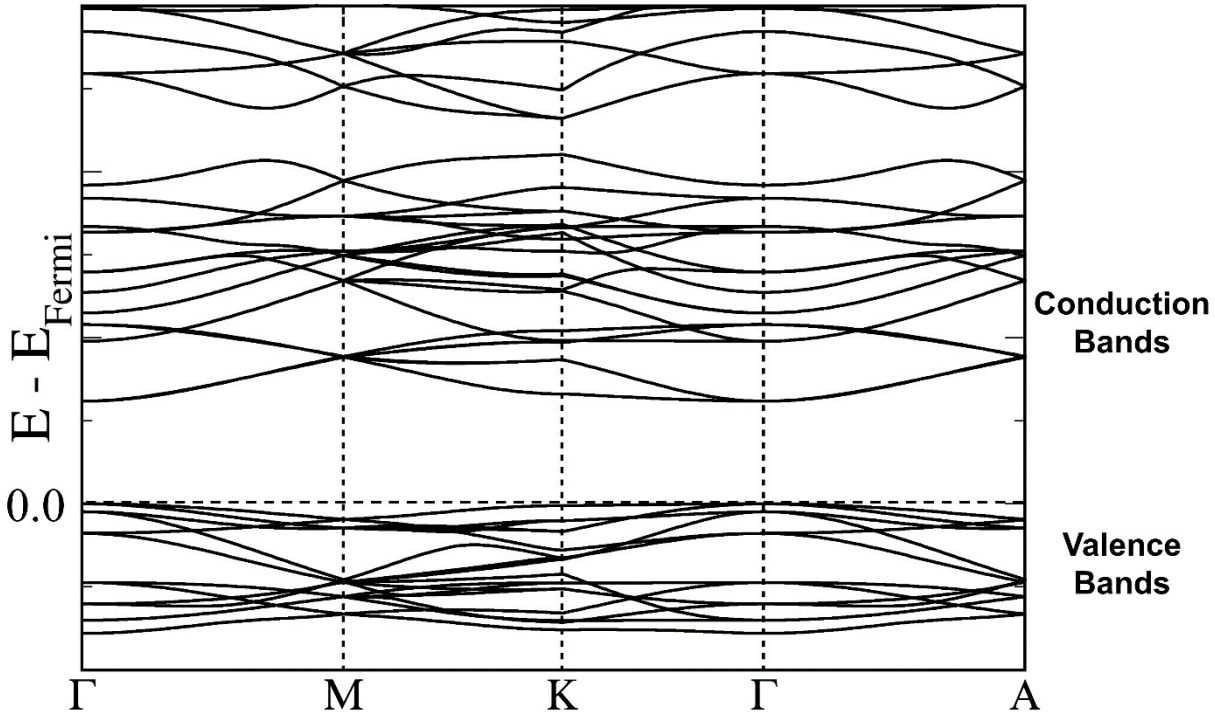

Fig. S17. The full band structure of cubic STO (in a rhombohedral cell with $R\bar{3}c$ space group symmetry and with zero tilting). All the bands have been aligned to the Fermi level.

References

1 A. V. Kovalevsky, A. A. Yaremchenko, S. Populoh, P. Thiel, D. P. Fagg, A. Weidenkaff and J. R. Frade, *Phys. Chem. Chem. Phys.*, 2014, **16**, 26946-26954.

2 H. Muta, K. Kurosaki and S. Yamanaka, *J. Alloys Compd.*, 2003, **350**, 292-295.

3 Y. A. Abramov, V. G. Tsirelson, V. E. Zavodnik, S. A. Ivanoc and I. D. Brown, *Acta Cryst. B*, 1995, **51**, 942-951.

4 A. A. Coelho, *J. Appl. Cryst.*, 2000, **33**, 899-908.

5 G. V. Chester and A. Thellung, *Proc. Phys. Soc.*, 1961, **77**, 1005-1013.

6 J. Callaway, *Phys. Rev.*, 1959, **113**, 1046-1051.

7 B. Abeles, *Phys. Rev.*, 1963, **131**, 1906-1911.

8 E. F. Steigmeier, *Phys. Rev.*, 1968, **168**, 523-530.

9 G. A. Slack and S. Galginaitis, *Phys. Rev.*, 1964, **133**, A253-A268.

10 Y. P. Joshi, *Physica Status Solidi B*, 1979, **95**.

11 R. A. Richardson, S. D. Peacor, C. Uher and F. Nori, *J. Appl. Phys.*, 1992, **72**, 4788-4791.

12 P. G. Klemens, *Proc. Phys. Soc. A*, 1955, **68**, 1113-1128.

13 J. Yang, D. T. Morelli, G. P. Meisner, W. Chen, J. S. Dyck and C. Uher, *Phys. Rev. B*, 2002, **65**, 094115.

14 T. M. Tritt, *Thermal Conductivity: Theory, Properties and Applications*, Kluwer Academic, New York, USA, 2004.

15 G. Dhanaraj, K. Byrappa, V. Prasad and M. Dudley, *Springer Handbook of Crystal Growth*, Springer, Heidelberg, Germany, 2010.

16 R. O. Pohl, *Phys. Rev. Lett.*, 1962, **8**, 481-483.

17 M. Ahrens, R. Merkle, B. Rahmati and J. Maier, *Phys. B*, 2007, **393**, 239-248.

18 D. G. Cahill, S. K. Watson and R. O. Pohl, *Phys. Rev. B*, 1992, **46**, 6131-6140.

19 W. Kaiser and R. Zurek, *Phys. Lett.*, 1966, **23**, 668-670**.**

20 C. B. Vining, *J. Appl. Phys.*, 1991, **69**, 11.

21 T. Okuda, K. Nakanishi, S. Miyasaka and Y. Tokura, *Phys. Rev. B*, 2001, **63**, 113104.

22 I. K. Dimitrov, M. E. Manley, S. M. Shapiro, J. Yang, W. Zhang, L. D. Chen, Q. Jie, G. Ehlers, A. Podlesnyak, J. Camacho and Q. Li, *Phys. Rev. B*, 2010, **82**, 174301.

23 R. P. Hermann, R. Jin, W. Schweika, F. Grandjean, D. Mandrus, B. C. Sales and G. J. Long, *Phys. Rev. Lett.*, 2003, **90**, 135505.

24 K. Suekuni, M. A. Avila, K. Umeo and T. Takabatake, *Phys. Rev. B*, 2007, **75**, 195210.

25 M. Drulis, R. Poprawski and J. MróZ, *Ferroelectrics*, 2004, **302**, 43-45.

26 B. Sattibabu, A. K. Bhatnagar, S. S. Samatham, D. Singh, S. Rayaprol, D. Das, V. Siruguri and V. Ganesan, *J. Alloys Compd.*, 2015, **644**, 830-835.

27 G. P. Malik, *Superconductivity: A New Approach Based on the Bethe-Salpeter Equation in the Mean-FIeld Approximation*, Vol. 21, World Scientific, Singapore, 2016.

28 C. Adamo and V. Barone, *J. Chem. Phys.*, 1999, **110**, 6158-6170.

29 R. Dovesi, R. Orlando, A. Erba, C. M. Zicovich-Wilson, B. Civalleri, S. Casassa, L. Maschio, M. Ferrabone, M. De La Pierre, P. D'Arco, Y. Noël, M. Causà, M. Rérat and B. Kirtman, *Int. J. Quantum Chem.*, 2014, **114**, 1287-1317.

30 R. Dovesi, V. R. Saunders, C. Roetti, R. Orlando, C. M. Zicovich-Wilson, F. Pascale, B. Civalleri, K. Doll, N. M. Harrison, I. J. Bush, P. D'Arco, M. Llunell, M. Causà and Y. Noël, CRYSTAL14 User's Manual (University of Torino, Torino, 2014), Available at http://www.crystal.unito.it.

31 J. Hutter, M. Iannuzzi, F. Schiffmann and J. VandeVondele, *Wiley Interdiscip. Rev.: Comput. Mol. Sci.*, 2014, **4**, 15-25.
32 J. P. Perdew, K. Burke and M. Ernzerhof, *Phys. Rev. Lett.*, 1996, **77**, 3865.
33 J. VandeVondele, M. Krack, F. Mohamed, M. Parrinello, T. Chassaing and J. Hutter, *Comput. Phys. Communications*, 2005, **167**, 103-128.
34 J. VandeVondele and J. Hutter, *J. Chem. Phys.*, 2007, **127**, 114105.
35 S. Godecker, M. Teter and J. Hutter, *Phys. Rev. B*, 1996, **54**, 1703.
36 M. Krack, *Theor. Chem. Acc.*, 2005, **114**, 145-152.
37 V. F. Sears, *Neutron News*, 1992, **3**, 26-37.
38 H. D. Megaw and C. N. W. Darlington, *Acta Cryst. A*, 1975, **31**, 161-173.
39 S. R. Popuri, A. J. M. Scott, R. A. Downie, M. A. Hall, E. Suard, R. Decourt, M. Pollet and J. W. G. Bos, *RSC Adv.*, 2014, **4**, 33720-33723.
40 T. Q. Thong, L. T. T. Huong and N. T. Tinh, *Mater. Trans.*, 2015, **56**, 1365-1369.
41 B. Zhang, J. Wang, T. Zou, S. Zhang, X. Yaer, N. Ding, C. Liu, L. Miao, Y. Li and Y. Wu, *J. Mater. Chem. C*, 2015, **3**, 11406-11411.